

RESEARCH ARTICLE | APRIL 18 2025

Ultrafast observation of shock wave formation in aluminum under direct femtosecond laser irradiation

Nobuhiko Nakanii (中新信彦) ; Yudai Mori (森祐大); Seiryu Inoue (井上聖流); Tomokazu Sano (佐野智一)

Check for updates

J. Appl. Phys. 137, 153108 (2025)
<https://doi.org/10.1063/5.0263267>



Articles You May Be Interested In

Direct measurement of lattice behavior during femtosecond laser-driven shock front formation in copper

J. Appl. Phys. (March 2025)

Non-contact ultrasonic acquisition of femtosecond laser-driven ablative Mbar-level shock waves on Ti alloy surface

Appl. Phys. Lett. (February 2016)

Elastoplastic and polymorphic transformations of iron at ultra-high strain rates in laser-driven shock waves

J. Appl. Phys. (December 2021)

19 April 2025 07:51:54



Nanotechnology & Materials Science



Optics & Photonics



Impedance Analysis



Scanning Probe Microscopy



Sensors



Failure Analysis & Semiconductors



Unlock the Full Spectrum. From DC to 8.5 GHz.

Your Application. Measured.

[Find out more](#)



Ultrafast observation of shock wave formation in aluminum under direct femtosecond laser irradiation

Cite as: J. Appl. Phys. **137**, 153108 (2025); doi: [10.1063/5.0263267](https://doi.org/10.1063/5.0263267)

Submitted: 4 February 2025 · Accepted: 1 April 2025 ·

Published Online: 18 April 2025



View Online



Export Citation



CrossMark

Nobuhiko Nakanii (中新信彦),^{1,2,a)}  Yudai Mori (森祐大),² Seiryu Inoue (井上聖流),²
and Tomokazu Sano (佐野智一)² 

AFFILIATIONS

¹Kansai Institute for Photon Science (KPSI), National Institutes for Quantum Science and Technology (QST), Kizugawa, Kyoto 619-0215, Japan

²Graduate School of Engineering, The University of Osaka, Yamada-oka 2-1, Suita, Osaka 565-0871, Japan

^{a)}Author to whom correspondence should be addressed: nakanii.nobuhiko@qst.go.jp

ABSTRACT

Shock wave formation in aluminum after the direct irradiation of a femtosecond laser pulse with an intensity of 10^{14} W/cm² onto the metal surface in air was observed using frequency-domain interferometry with picosecond temporal resolution. This high resolution allows us to accurately evaluate arrival time and rise time of the wave before and after shock wave formation. The temporal evolution of the rear surface velocity of the metal film had an ultrafast rise at the wavefront of less than 5 ps and a two-wave structure. As the incident pump laser energy decreased or the metal film thickness increased, the amplitude of the first wave decayed and the time separation between the two waves increased. The relationship between the particle velocity and shock velocity indicated that aluminum was elastically compressed in a longitudinal stress of 185 GPa, reaching a strain of approximately 30%. The estimated elastic strain rate was 6×10^{10} s⁻¹ at 500 nm in depth. Through a thermal nonequilibrium state in the early stage, aluminum becomes a metastable elastic Hugoniot state under such high longitudinal stress in a region deeper than the diffusion length of laser-heated electrons.

© 2025 Author(s). All article content, except where otherwise noted, is licensed under a Creative Commons Attribution (CC BY) license (<https://creativecommons.org/licenses/by/4.0/>). <https://doi.org/10.1063/5.0263267>

I. INTRODUCTION

Intense laser-driven shock waves are of scientific interest for replicating high-pressure conditions found on planets and are also crucial for industrial applications such as laser peening, which enhances and restores material properties.^{1–3} Femtosecond laser-driven shock waves (fs shocks) can deliver an instantaneous high pressure in a material. Laser peening with fs shocks can generate sufficient pressure to modify material properties without plasma confinement by a layer of transparent material such as water. A sacrificial layer on the material surface is also unnecessary because the thermal effect is much lower than that in conventional peening using a nanosecond laser pulse. Peening with direct irradiation of femtosecond laser pulses is known as dry laser peening (DLP).^{4,5} The DLP can improve fatigue properties of a metal specimen with hardening and the addition of compressive residual stress. The

improvement of fatigue properties is caused by the formation of unique microstructures, including high-density lattice defects.^{6,7} Moreover, fs shocks not only enhance and restore mechanical properties but also induce unique phenomena such as quenching high-pressure phases, which do not appear in the conventional method based on nanosecond laser-driven shock waves.⁸ Understanding the unique phenomena resulting from fs shocks is of interest in physics and is expected to contribute to further improvements in the properties of metals.

The initial pressure generated by the direct irradiation of a femtosecond laser pulse on a metal surface has been estimated to reach several terapascals. This pressure was derived by extrapolating the velocity of a blast wave that propagates steadily through the air. However, using this method to estimate the pressure in the interaction region near the metal surface is not appropriate because

19 April 2025 07:51:54

nonlinear and transient phenomena dominate in this region.⁹ Frequency-domain interferometry (FDI) has been used in various fields to observe ultrafast phenomena by detecting the relative phase difference between two broadband ultrashort laser pulses.^{10,11} This method allows us to characterize the transient state inside a material compressed by fs shocks.^{12–16} The first demonstration by Evans *et al.*¹² estimated the pressure of aluminum under a shock wave driven by a 120 fs laser pulse of 10^{14} W/cm² to be 100–300 GPa along the SESAME (3717) Hugoniot curve for aluminum. Numerous research groups have conducted FDI to investigate compressed states of various materials with diverse laser parameters. Metallic thin films coated on glass substrates were used as the targets in these studies. In most of the works, pump laser pulse irradiated to the metal film through the glass substrate to confine ablated plasma, thereby producing high pressure. For this plasma confinement scheme, the laser pulse intensities should be low to avoid breakdown or ionization in the transparent layer. Only Evans *et al.*¹² performed FDI on the direct irradiation of a high-intensity laser pulse on the metal surface. This configuration is the same as that of DLP and the microstructure formation with fs shocks. The behavior of the fs shock could have an important role in both DLP and the microstructure formation.¹⁷ Gahagan *et al.*¹⁴ observed an ultrafast rise of the fs shock front within 6.25 ps and induced pressures ranging from 3 to 5 GPa in a plasma confinement geometry, where the laser pulse was irradiated to a metal through quartz. The estimated strain rate exceeded 10^{10} s⁻¹. In a direct irradiation geometry, the initial behavior of the shock wave, such as the ultrafast rise of the shock front, has never been measured with picosecond-order high-temporal resolution.

The time interval of the probe pulse pair in FDI determines the temporal resolution and the sensitivity to phase shifts. A long-time interval of the probe pair can easily detect the phase shift because the displacement of the reflecting surface is large during the probe interval. However, the ultrafast temporal variation in the surface motion can disappear. Increasing the interval of the probe pair reduces the gradient of the rise time.¹⁸ The rise time of the surface velocity is one of the important parameters related to the strain rate of the material. Furthermore, a large interval of the probe pair may cause measurement deviations in the arrival time of the shock wave at the rear surface, which affects the shock velocity. To precisely resolve the ultrafast behavior of fs shocks, an ultra-short interval in the probe pulse pair is necessary.

In this study, we aimed to investigate the shock wave formation process in aluminum driven by the direct irradiation of an intense femtosecond laser pulse. We performed high-temporal-resolution FDI using a short-interval probe pulse pair to measure the particle velocity in a compressed region behind the wavefront and the wave propagation velocity, including the shock velocity, by observing the rear surface motion as the wave breaks through. The material state before and after shock wave formation was investigated by comparing the relationship between the particle velocity and the wave propagation velocity in the measurement with the well-known relationship between the particle velocity and shock velocity under the Hugoniot state investigated in previous studies. The pump laser pulse was directly irradiated to the metal surface at an intensity above 10^{14} W/cm² in an atmosphere environment. The time evolution of the velocity of the metal rear surface attached to a

glass substrate was measured for several film thicknesses. The short time interval of 1.3 ps between two probe pulses, which was one order of magnitude less than 18 ps in the previous work by Evans *et al.*,¹² allowed to resolve the steep rise time of the wavefront and accurately determine the arrival time. Our experimental results suggest that aluminum transitions into a metastable elastic Hugoniot state with extremely high longitudinal stress through an initial thermal nonequilibrium before plastic deformation, rather than the conventional plastic Hugoniot state as presented by Evans *et al.* This longitudinal stress was much higher than that observed by Ashitkov *et al.*¹³ using the plasma confinement scheme. Such behavior of the shock wave could lead to unique properties in materials given by the direct irradiation of the femtosecond laser pulse on the metal in the air.

II. EXPERIMENTAL SETUP

The experimental setup is illustrated in Fig. 1(a). The setup and conditions were similar to those adopted in Ref. 12. Laser pulses were delivered from Spectra Physics Solstice ACE, which was a kilohertz Ti:sapphire laser system with chirped pulse amplification. The laser pulse had a Gaussian spatial distribution with $M^2 < 1.25$ and a diameter of ~ 10 mm in $1/e^2$. The central wavelength was 800 nm, and the contrast ratio between the main pulse and nanosecond pre-pulse was approximately 10^{-3} . The pulse duration was optimized to 93 fs before the focal lens of the pump pulse. The repetition rate of the laser pulse was reduced to 10 Hz by using a fast Pockels cell, after which a single pulse was selected by a mechanical shutter driven by a single-shot transistor-transistor-logic (TTL) trigger synchronized with the laser pulse. The laser pulse was split by a 90:10 beam splitter to a pump pulse for driving the shock wave and a probe pulse for FDI.

The pump pulse was focused by a plano-convex singlet lens with a 70 mm focal length and irradiated to a thin aluminum film coated on a glass substrate by vacuum deposition. The aluminum film thicknesses were 60, 250, and 500 nm. The substrate was made of optical borosilicate glass (BK7) and had a thickness of 8 mm and a diameter of 50 mm. The other surface of the glass substrate had antireflective coating for the 800 nm wavelength to prevent reflection of probe pulses from the glass surface (excluding the 60 nm aluminum film target). Following each laser irradiation, the target slid for the next irradiation on the new metal surface. The aluminum coated by vacuum deposition has a polycrystalline structure with submicron crystalline size, which is smaller than the laser spot and sufficiently homogenous.

The energies of pump pulses were 1 and 5 mJ. An attenuator consisting of a half-wave plate and a polarizer adjusted the pump pulse energy and rotated the polarization of the pump pulse to be perpendicular to that of the probe pulse. As shown in Figs. 1(b) and 1(c), the spot sizes of the pump pulses on the target surface were estimated from the irradiation area diameter and were 90 and 180 μ m for 1 and 5 mJ, respectively. The focusing of a high-intensity laser pulse in the atmosphere induced nonlinear effects and breakdown, making direct observation of the focal spot impossible. The nonlinear effects complicated the laser propagation, and the laser pulse could not be focused on the diffraction limit.¹⁹ The irradiation area sizes were ~ 10 times larger than the diffraction

19 April 2025 07:51:54

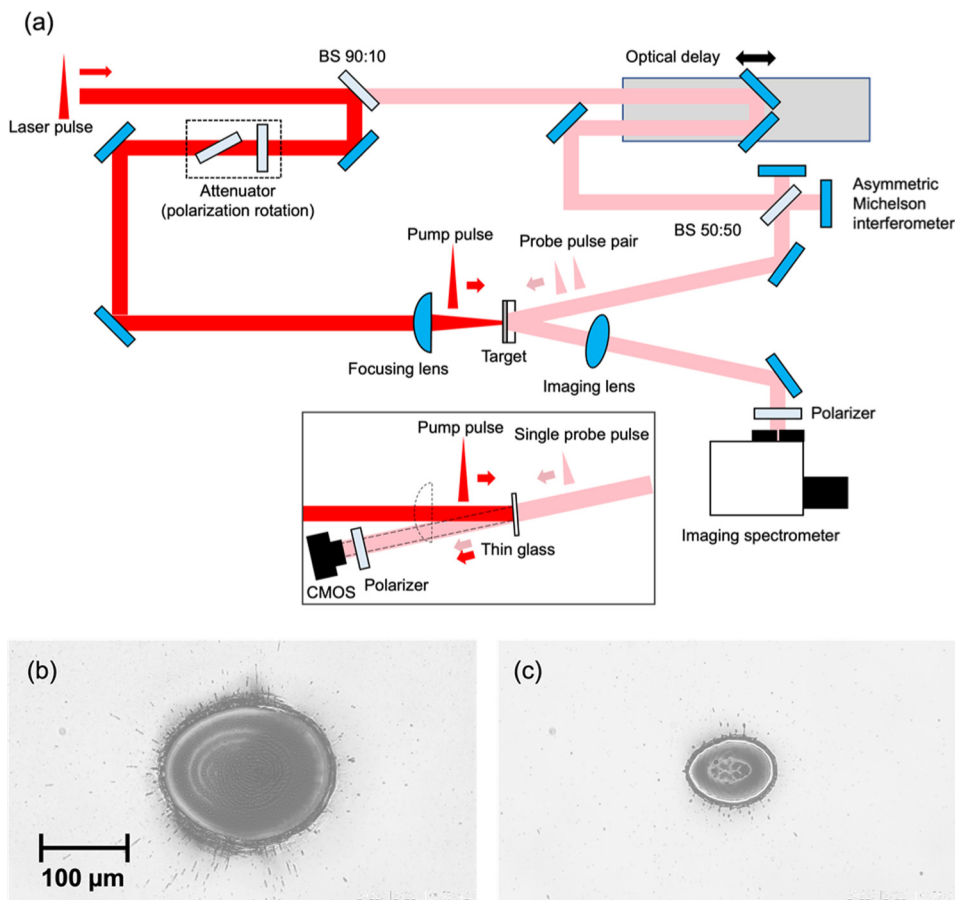


FIG. 1. (a) Schematic of the ultrafast FDI experiment to investigate the compressed state of the metal under intense fs shock. The inset shows the setup for determining the zero delay by observing the interference fringe between the pump pulse and the first probe pulse. Microscopic images of surfaces of 500 nm aluminum film targets obtained by optical microscopy after femtosecond laser pulse irradiation with pulse energies of (b) 5 and (c) 1 mJ.

limit. The corresponding intensities of pump pulses were 1.7×10^{14} and 2.1×10^{14} W/cm², respectively. During such high-intensity laser irradiation on the metal surface, the partial energy of the laser pulse is absorbed by electrons in the skin depth of metal owing to the inverse Bremsstrahlung. The energy of heated electrons is diffused to nearby cold electrons through collisions. The temperature of the electrons could reach 70–90 eV; in contrast, that of the ions remains low, resulting in a two-temperature state. Following this, energy relaxation from the electrons to the ions occurs. The estimated lattice temperature of the film in thermal equilibrium after electron–phonon coupling could be 50–70 eV.²⁰

The probe pulse was split into two pulses with a time delay through an asymmetric Michelson interferometer. The probe pulse pair was irradiated to the rear surface of the aluminum film with a 14.5° incident angle through the glass substrate. The reflection of the probe pulse pair was detected on a charge-coupled device (Princeton Instruments PIXIS 400) in an imaging spectrometer (Acton Research SpectraPro 2300i). The slit width of the imaging spectrometer was 50 μm. The rear surface of the film was imaged to the slit at the entrance of the imaging spectrometer with a magnification of 7.1 by an achromatic lens. To observe the ultrafast behavior of the metal surface with picosecond resolution, the time gap between the probe

pulse pair was set to 1.3 ps. The irradiation timing of the probe pulse pair for the pump pulse was adjusted with an optical delay. The step of the optical delay scan was set to 0.67 ps. The phase shift between two probe pulses was extracted from the interferogram in the spectrum by applying the Fourier transform.^{10,11}

Zero delay of the probing was defined as the time of pump laser irradiation at the metal front surface and was determined by the optical interference between the pump pulse and the first pulse of the probe pair. The focus lens for the pump pulse was removed, and the target was replaced by a thin transparent cover glass as illustrated in the inset in Fig. 1(a). The surface of the cover glass on the pump irradiation side was adjusted to the same position as the metal surface of the target. The reflection of the pump pulse and the transmission of the first probe pulse overlapped on a complementary metal–oxide–semiconductor (CMOS). Inserting a polarizer with a 45° polarization axis for the pump pulse and the first probe pulse in front of the CMOS induced an interference fringe caused by the two pulses with mutually orthogonal polarizations. The zero delay was determined by observing the timing of the interference, taking into account the thickness and the refraction index of the transparent optics, including the lens, the substrate, and the cover glass.

III. RESULTS AND DISCUSSION

Figures 2(a) and 2(b) show the temporal evolution of the rear surface velocity for the metal film for 5 and 1 mJ pump laser energies, respectively. The surface velocity of the rear surface of the metal film is obtained as

$$u_{sf} = \frac{\lambda_0}{4\pi n \cos\theta} \frac{\Delta\phi}{\Delta t}, \quad (1)$$

where $\Delta\phi$, Δt , λ_0 , n , and θ are the phase shift, the time interval of the probe pair, the central wavelength of the probe pulses, the refractive index of the transparent substrate, and the incident angle of the probe pulses, respectively. Figures 2(c) and 2(d) show the spatial distribution of phase shift at the first local peak (or the first inflection point) in the temporal evolution. The spatial distribution of the phase shift was relatively uniform with a super-Gaussian like distribution. The nonlinear effect during the focusing of the femtosecond laser pulse in the air led to the focusing waist being formed upstream of the vacuum focal point and becoming much larger than the diffraction limit. The intensity (or fluence) distribution at the waist point became more uniform than that at the focal point in the vacuum.¹⁹ This uniform distribution of the laser fluence could be the reason for the uniform formation of the shock wave.

The surface velocity shown in Figs. 2(a) and 2(b) was obtained from the spatial average of the phase shift in 80% of the laser spot diameter, and the error bar indicates its standard deviation. The waveform of the surface velocity varies significantly with the film thickness. For a 60 nm film, a steep and large velocity change was observed immediately after laser irradiation. At 1 mJ laser energy for the 60 nm film, two waves appeared in the rising such that the

precursor elastic wave was followed by a plastic wave. By increasing the laser energy to 5 mJ, both waves reached almost simultaneously, and the secondary wave came before the velocity decreased. For all films thicker than 250 nm, the two waves were completely separated. The surface velocity increased and dropped quickly, and it increased again after approximately 20 ps. By decreasing the incident pump laser energy or increasing the target thickness, the time separation between the two waves increased, the wave amplitudes decayed, and the rising and falling slopes became gradual.^{21,22} This kind of time trend of the rear surface motion has never been observed in the direct irradiation geometry of fs shock studies.

To examine the material state after the intense femtosecond laser irradiation, particle velocity u_p and wave propagation velocity U_{wp} were evaluated from the temporal evolution of the surface velocity. Figure 3 shows the u_p - U_{wp} relationship of the experimental data. The particle velocity was calculated from the maximum surface velocity, which was obtained from the first local peak or the first inflection point in Figs. 2(a) and 2(b).¹⁸ If the rear side of the target is a free surface without any substrates, the maximum surface velocity becomes approximately twice the particle velocity.²³ In our case, this assumption cannot be used because the rear surface of the metal was attached to the glass substrate. The shock impedance mismatching between aluminum and BK7 glass satisfies

$$u_p = \frac{Z_{Al} + Z_{BK7}}{2Z_{Al}} u_{sf0}, \quad (2)$$

where u_{sf0} is the maximum surface velocity and Z_i is the shock impedance of material i . The particle velocity became 92% of the peak surface velocity using the shock impedance of both materials

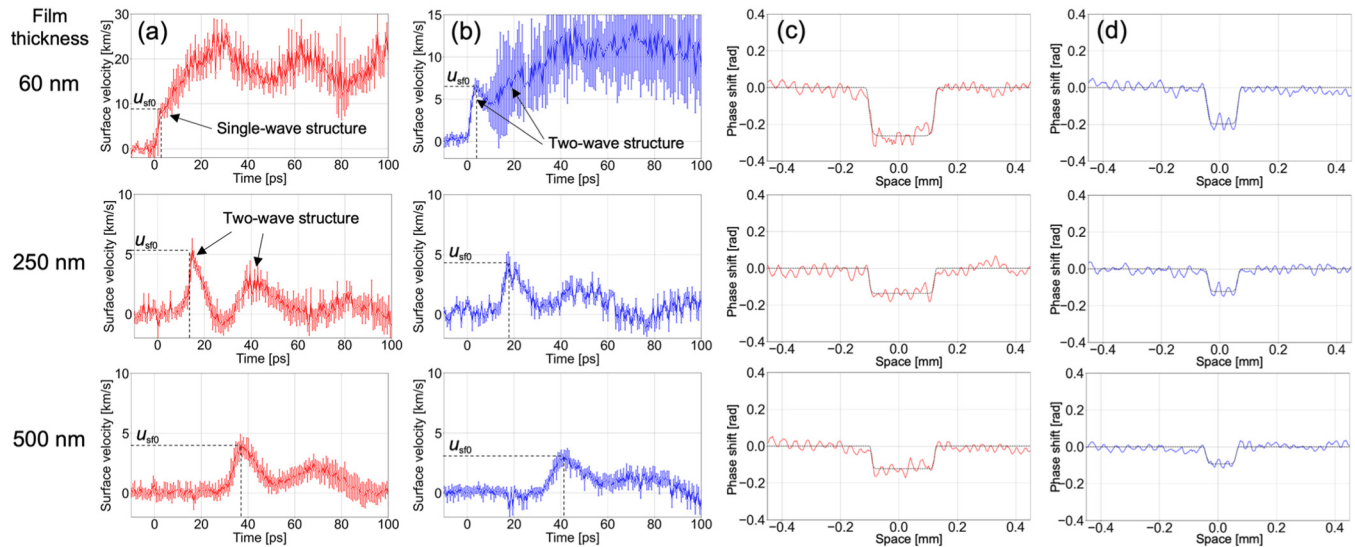


FIG. 2. Temporal evolution of rear surface velocities of the aluminum film obtained from phase shift during probe pulse pair for (a) 5 and (b) 1 mJ pump laser energies. Spatial distribution of phase shift at the first local peak (or the first inflection point) in temporal evolution for (c) 5 and (d) 1 mJ laser energies with a super-Gaussian fitting curve (black dashed curve). The graphs at the top, middle, and bottom indicate film thicknesses of 60, 250, and 500 nm, respectively. The surface velocity in (a) and (b) is obtained from the spatial average of phase shift in the region of 80% of the laser spot diameter, and the error bar indicates the corresponding standard deviation.

19 April 2025 07:51:54

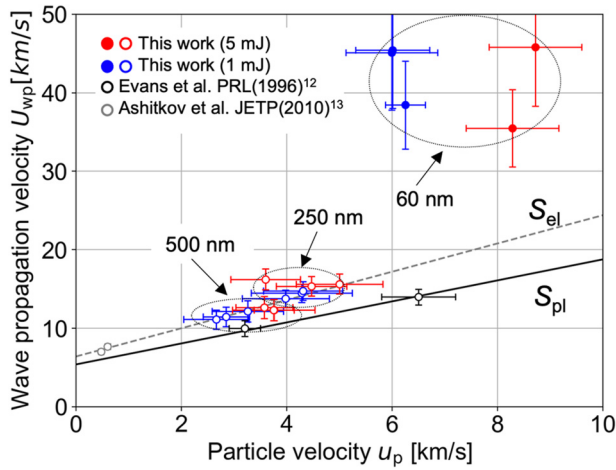


FIG. 3. Relationship between the particle velocity u_p and wave propagation velocity U_{wp} at 5 (red) and 1 mJ (blue) laser energies. The closed and open circles indicate the plots before and after shock wave formation, respectively. Only the wave propagation velocities shown as open circles correspond to shock velocity U_s . The experimental results by Evans *et al.*¹² (black open) and Ashitkov *et al.*¹³ (gray open) are also shown. The lines indicate the plastic Hugoniot relation (black solid line) and the elastic Hugoniot relation under uniaxial elastic compression (gray dashed line).

in Ref. 24. As the shock impedances were approximately the same, the shock wave reflection should be considerably weaker than the free-surface reflection, and the shock wave should maintain its velocity when traveling from aluminum to BK7.²⁵ Hence, we can observe a situation that resembles the conditions inside the metal. The wave propagation velocity was obtained from the arrival time difference divided by the thickness difference of the films as

$$U_{wp}(d_n) = \frac{d_n - \overline{d_{n-1}}}{t_n - \overline{t_{n-1}}}, \quad (3)$$

where d is the film thickness, t is the measured arrival time of the wavefront, which is the time at half of the first local peak (or the first inflection point) during the surface velocity rising, and subscript n indicates the thickness, with d_n being 60, 250, and 500 nm for $n = 1, 2,$ and $3,$ respectively. For $n = 0,$ we set $d_0 = 0$ and $t_0 = 0,$ which is the zero delay determined by the interference. The overline indicates the average value for each condition.

The error of each parameter in Fig. 3 was calculated according to the error propagation law. The error of wave propagation velocity was obtained from the measurement error of the film thickness and accuracy of the arrival time. The measurement error of the film thickness with a quartz crystal unit was $\pm 5\%$. The accuracy of the arrival time was ± 149 fs, which was determined by the position accuracies of an optical delay stage ($\pm 20 \mu\text{m}$) and a target stage ($\pm 10 \mu\text{m}$), and the surface accuracy of the target (± 800 nm). The particle velocity error was calculated from the spatial fluctuation of the measured phase shift, which corresponds to the vertical error bar at the maximum surface velocity in Fig. 2. This was the most

dominant factor of the particle velocity error. The errors of the central wavelength ($\pm 0.5\%$), the refractive index of the glass substrate ($\pm 0.05\%$), the cosine of the probe incident angle ($\pm 0.37\%$), and the time interval between the probe pair (~ 40 fs corresponding to a single bin size in the time domain after inverted Fourier transform) were also considered in this error of the particle velocity. The errors of shock impedances of materials were not considered because they were unknown. The phase measurement accuracy of FDI ($\pm 0.05\%$)¹¹ was also negligible for the spatial fluctuation.

The black solid (S_{pl}) and gray dashed (S_{el}) lines in Fig. 3 indicate the plastic Hugoniot relation of aluminum bulk, $U_{S(pl)} = 5.386 + 1.339u_p$,²⁶ and elastic Hugoniot relation under uniaxial elastic compression, $U_{S(el)} = 6.4 + 1.8u_p$,¹³ respectively. The Hugoniot state is a thermodynamically equilibrium shocked state.^{27,28} The plots at 60 nm in depth, shown as closed circles in Fig. 3, clearly deviated from the elastic and plastic Hugoniot relations. As mentioned in Sec. II, the energy transfers from the high-intensity laser pulse to the electrons in the skin depth through the inverse Bremsstrahlung, and the heated electrons are diffused by electron–electron collisions. The energy relaxation from electrons to ions occurs with a slight delay after electron diffusion. This thermal diffusion length of electrons was estimated to be ~ 80 nm in our experimental conditions,²⁹ being slightly longer than the thinnest thickness of 60 nm. In this case, the electron diffusion reached the rear surface of the metal film, and energy transfer from electrons to ions occurred even on the rear surface. As the estimated relaxation time was ~ 2 ps, the motion on the rear surface began within this period after laser irradiation. Hence, the shock wave has not been formed yet for the thinnest film. The time until the rear surface motion was obviously shorter than the arrival time of the shock wave estimated from the shock velocity on the Hugoniot state. The wave propagation velocities in both cases for 5 and 1 mJ were ~ 40 km/s, almost corresponding to the thermal diffusion length divided by the relaxation time. This wave propagation velocity can be called the thermal wave velocity instead of the shock velocity. For such a thin film, the thermal wave can perturb the rear surface.^{12,30} The deviation of the wave propagation velocities from the elastic and plastic Hugoniot relations could be attributed to other factors, such as surface roughness or film adhesion to the substrate. However, the targets were commercial high-grade optical mirrors (Sigma Koki TFAN series). The surface roughness of such an optical mirror is small (less than 1 nm), and the adhesion between the substrate and the film coated via the vacuum deposition is also strong. These should not contribute to the large deviation from the Hugoniot relations.

The plots at depths above 250 nm are shown as red and blue open circles in Fig. 3. All the plots except for one are on the elastic Hugoniot line. Deeper than the electron diffusion length and after the relaxation time of electron–phonon coupling, the electrons and ions were in thermal equilibrium. In this situation, the shock wave was formed, and the wave propagation velocity indicated the shock velocity U_s . The transfer region between thermal wave behavior and shock wave formation is important to evaluate the shock velocity and should influence the results for the 250 nm film because the shock velocity at 250 nm was the average velocity in the distance from 60 to 250 nm, where the transfer region could exist. The thinnest film thickness of 60 nm is similar value to the thermal

19 April 2025 07:51:54

diffusion length, which could be close to be the transfer region. Therefore, the error of shock velocity at 250 nm should be small. Moreover, the thermal diffusion length depends on absorbed laser energy per unit area in the skin depth, which is proportional to the irradiated laser fluence. In our experimental conditions, the thermal diffusion length should be maintained because there was no significant difference in the laser fluence. To investigate the details around the transient region and evaluate the shock velocity more precisely, observations of varying thicknesses with fine steps are required.

The longitudinal stress under elastic Hugoniot can be obtained as

$$\sigma_z = \rho_0 U_S u_p, \quad (4)$$

where z indicates the shock wave propagation direction, ρ_0 is the initial density of aluminum (2710 kg/m^3), and u_p and U_S are the corresponding measurements. The longitudinal stresses at 250 nm in depth were 185 and 163 GPa and decreased to 124 and 92 GPa at 500 nm for laser energies of 5 and 1 mJ, respectively. The metal strain can be evaluated from the ratio of particle velocity to shock velocity, $\varepsilon = u_p/U_S$. The elastic strain reached 29.3% for a 500 nm thick target at 5 mJ laser energy. The longitudinal stress for a compression ratio of volume given by $V/V_0 = 1 - \varepsilon$ is shown in Fig. 4. The errors of the longitudinal stress and the volume compression ratio were calculated from the estimated error of the film density (-10%) and the errors of shock velocity and particle velocity in Fig. 3.

The pressure on the plastic Hugoniot curve p_H at the same compression ratio as the elastic compression can be obtained using elastic strain ε as follows:

$$p_H = \frac{\rho_0 \varepsilon c_0^2}{(1 - \varepsilon)^2}, \quad (5)$$

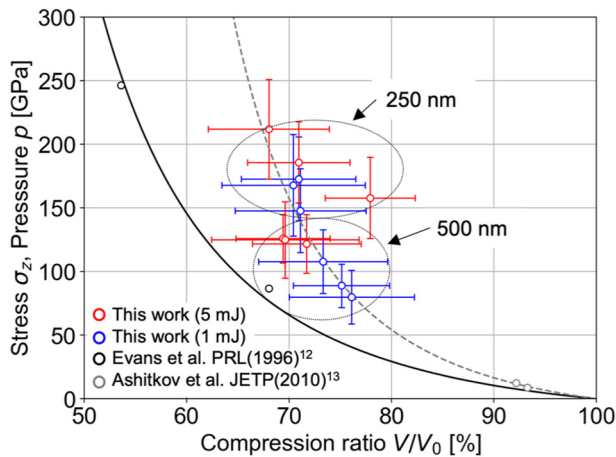


FIG. 4. Longitudinal stress and pressure according to compressed volume under fs shocks. The definitions of plots and lines are the same as those in Fig. 3.

where c_0 and s are the bulk sound speed and the coefficient, respectively, in the u_p-U_S relation on the plastic Hugoniot, given by $U_{S(p)} = c_0 + su_p$. For the aluminum bulk, $c_0 = 5.386 \text{ km/s}$ and $s = 1.339$. The maximum shear stress τ is determined from the difference between longitudinal stress σ_z in elastic compression and pressure p_H on the plastic Hugoniot state at the same specific volume,^{13,23}

$$\sigma_z(V) - p_H(V) = \frac{4}{3} \tau. \quad (6)$$

The measured longitudinal stress, calculated pressure on the plastic Hugoniot curve at a given specific volume, and maximum shear stress are listed in Table I. The large shear stresses of 98 and 76 GPa for 250 nm in depth were mitigated during propagation and eventually dropped to 45 and 35 GPa for 500 nm in depth at 5 and 1 mJ laser energies, respectively.

The rise time of the shock wave Δt , which was defined as the time from 10% to 90% of the first local peak, was 3.9 and 4.8 ps for 250 and 500 nm in depth at 5 mJ laser energy. At 1 mJ laser energy, the rise time was 4.8 and 7.2 ps for 250 and 500 nm in depth, respectively. These values agree with results from previous studies on the fs shocks with the plasma confinement scheme.^{14,15} The rise time increases with increasing target thickness and decreasing pump laser energy. A probe pair with a short time gap of 1.3 ps allowed to resolve the picosecond-order ultrafast rise. The compressive strain rate $\dot{\varepsilon}$ can be estimated by the elastic strain divided by the rise time of the shock wave,

$$\dot{\varepsilon} = \varepsilon/\Delta t. \quad (7)$$

The strain rate in the elastic compression obtained from the ultra-short rise time reached $6.2 \times 10^{10} \text{ s}^{-1}$ at 500 nm. The strain rate also decreased with decreasing pump laser energy and increasing target thickness.

By shortening the interval of the probe pair, we succeeded to obtain a detailed waveform with high-temporal resolution. The ultrafast rise of less than 5 ps and the two-wave structure have not been observed in the experiment by Evans *et al.* Moreover, while their plots of the particle velocity and the shock velocity were placed on the plastic Hugoniot line, our results were on the extension of the elastic Hugoniot line presented by Ashitkov *et al.* The shock velocity and the particle velocity measured in our experiment were much faster than those obtained by Ashitkov *et al.* using the plasma confinement scheme. This means that the metastable elastic compression with considerably higher longitudinal stress was achieved by the direct irradiation scheme.

The temporal profile of the surface velocity shown in Fig. 2 indicated that the shock wave induced by the direct irradiation of a high-intensity fs laser pulse had a two-wave structure like the elastic-plastic structure consisting of a leading elastic wave with the following plastic deformation.^{21,31,32} Moreover, the results suggested the fs shock with the direct irradiation scheme had a metastable elastic compression zone with extremely high longitudinal stress, which is much higher than the general elastic limit. These results are consistent with direct observations of the lattice behavior

19 April 2025 07:51:54

TABLE I. Average longitudinal stress, calculated pressure on plastic Hugoniot curve at a given specific volume, and maximum shear stress. The superscript and subscript of the longitudinal stress indicate the differences from the average value to the measured maximum and minimum, respectively.

Film thickness (nm)	Laser energy (mJ)	Longitudinal stress σ_z (GPa)	Pressure at Hugoniot state p_H (GPa)	Shear stress τ (GPa)
250	5	185^{+26}_{-27}	55	98
250	1	163^{+10}_{-15}	62	76
500	5	124^{+1}_{-2}	65	45
500	1	92^{+15}_{-12}	45	35

of a metal under fs shock obtained from x-ray free-electron laser diffraction.^{17,33} During the ultrashort time before starting the plastic deformation, the large shear stress could exist. By this large shear stress, the metastable elastic state could decay through the formation and multiplication of dislocations,³⁴ and the elastic state transitioned to the plastic state.³¹ In the case of nanosecond laser-driven shock waves, if the stress significantly exceeds the elastic limit, the plastic wave overlaps the elastic wave and the single wave is reached. The behavior of the fs shock significantly differed from that of the nanosecond laser-driven shock wave. This could lead to unique properties in materials given by the direct irradiation of the femtosecond laser pulse.

IV. CONCLUSION

The ultrafast behavior of aluminum under direct irradiation with a femtosecond laser pulse of 2×10^{14} W/cm² in the air was observed by FDI using a probe pulse pair with a picosecond time interval. The high-temporal resolution of the measurements allowed us to clearly describe the shock wave formation in a material by evaluating the velocity and the starting time of rear surface motion. The temporal evolution of the rear surface velocity of aluminum films with thicknesses ranging from 60 to 500 nm indicated an ultrafast rise at the wavefront of less than 5 ps and a two-wave structure. By either decreasing incident pump laser energy or increasing target thickness, the amplitude of the first wave decayed and the time separation between two waves became large. The relationship between the particle velocity and the wave propagation velocity obviously deviated from the Hugoniot curves at regions shallower than the thermal diffusion length, while the relation agreed with the elastic Hugoniot curve when reaching deeper than that length. The longitudinal stress in an elastically compressed aluminum under fs shock was 185 GPa, and the elastic strain was ~30%. The elastic strain rate reached approximately 6×10^{10} s⁻¹ at 500 nm in depth. These experimental results suggested that through the thermal nonequilibrium state in the early stage, the shock wave had a two-wave structure consisting of a leading elastic front followed by plastic deformation. The first elastic shock zone was the metastable state with a large longitudinal stress on the elastic Hugoniot curve. This indicates that the extremely high shear stress could exist before the plastic deformation. We suggest that the large shear stress in the elastic compression could produce high-density lattice defects in the transition from the elastic to the plastic state. Such a phenomenon cannot be observed with conventional nanosecond laser-driven shock waves.^{7,8}

ACKNOWLEDGMENTS

This study was supported by MEXT Quantum Leap Flagship Program (MEXT Q-LEAP) under Grant No. JPMXS0118068348. We thank Dr. M. Kando and Dr. Ko Kondo for their fruitful discussions and encouragement. We also received support from JSPS KAKENHI under Grant Nos. 19K22061, 20H02048, and 24K21579, Amada Foundation, Light Metal Educational Foundation, Inc., Osawa Scientific Studies Grants Foundation, Mazak Foundation, and Suzuki Foundation.

AUTHOR DECLARATIONS

Conflict of Interest

The authors have no conflicts to disclose.

Author Contributions

Nobuhiko Nakanii (中新信彦): Conceptualization (equal); Data curation (equal); Formal analysis (equal); Methodology (equal); Resources (equal); Software (equal); Validation (equal); Visualization (equal); Writing – original draft (equal); Writing – review & editing (equal). **Yudai Mori** (森祐大): Formal analysis (equal); Investigation (equal); Methodology (equal). **Seiryu Inoue** (井上聖流): Formal analysis (equal); Investigation (equal); Methodology (equal). **Tomokazu Sano** (佐野智一): Conceptualization (equal); Formal analysis (equal); Funding acquisition (equal); Investigation (equal); Methodology (equal); Project administration (equal); Resources (equal); Supervision (equal); Writing – original draft (equal); Writing – review & editing (equal).

DATA AVAILABILITY

The data that support the findings of this study are available from the corresponding author upon reasonable request.

REFERENCES

- P. Beck, P. Gillet, A. El Goresy, and S. Mostefaoui, *Nature* **435**, 1071–1074 (2005).
- R. P. Drake, *High-energy-density Physics: Fundamentals, Inertial Fusion, and Experimental Astrophysics* (Springer, 2006).
- R. D. Tenaglia and D. F. Lahrman, *Nat. Photonics* **3**, 267–270 (2009).
- T. Sano, T. Eimura, R. Kashiwabara, T. Matsuda, Y. Isshiki, A. Hirose, S. Tsutsumi, K. Arakawa, T. Hashimoto, K. Masaki, and Y. Sano, *J. Laser Appl.* **29**, 012005 (2017).
- M. Yoshida, I. Nishibata, T. Matsuda, Y. Ito, N. Sugita, A. Shiro, T. Shobu, K. Arakawa, A. Hirose, and T. Sano, *J. Appl. Phys.* **132**, 075101 (2022).

19 April 2025 07:51:54

- ⁶T. Matsuda, T. Sano, K. Arakawa, and A. Hirose, *Appl. Phys. Lett.* **105**, 021902 (2014).
- ⁷T. Matsuda, T. Sano, K. Arakawa, and A. Hirose, *J. Appl. Phys.* **116**, 183506 (2014).
- ⁸T. Sano, H. Mori, E. Ohmura, and I. Miyamoto, *Appl. Phys. Lett.* **83**, 3498–3500 (2003).
- ⁹A. A. Ionin, S. I. Kudryashov, S. V. Makarov, L. V. Seleznev, and D. V. Sinitsyn, *JETP Lett.* **94**, 34–38 (2011).
- ¹⁰E. Tokunaga, A. Terasaki, and T. Kobayashi, *Opt. Lett.* **17**, 1131–1133 (1992).
- ¹¹J. P. Geindre, P. Audebert, A. Rousse, F. Fallières, J. C. Gauthier, A. Mysyrowicz, A. D. Santos, G. Hamoniaux, and A. Antonetti, *Opt. Lett.* **19**, 1997–1999 (1994).
- ¹²R. Evans, A. D. Badger, F. Fallières, M. Mahdiah, T. A. Hall, P. Audebert, J.-P. Geindre, J.-C. Gauthier, A. Mysyrowicz, G. Grillon, and A. Antonetti, *Phys. Rev. Lett.* **77**, 3359–3362 (1996).
- ¹³S. I. Ashitkov, M. B. Agranat, G. I. Kanel', P. S. Komarov, and V. E. Fortov, *JETP Lett.* **92**, 516–520 (2010).
- ¹⁴K. T. Gahagan, D. S. Moore, D. J. Funk, R. L. Rabie, S. J. Buelow, and J. W. Nicholson, *Phys. Rev. Lett.* **85**, 3205–3208 (2000).
- ¹⁵D. J. Funk, D. S. Moore, K. T. Gahagan, S. J. Buelow, J. H. Reho, G. L. Fisher, and R. L. Rabie, *Phys. Rev. B* **64**, 115114 (2001).
- ¹⁶J. P. Chen, R. X. Li, Z. N. Zeng, X. T. Wang, W. Y. Wang, Y. H. Jiang, C. F. Cheng, and Z. Z. Xu, *J. Appl. Phys.* **94**, 858–862 (2003).
- ¹⁷T. Sano, T. Matsuda, A. Hirose, M. Ohata, T. Terai, T. Kakeshita, Y. Inubushi, T. Sato, K. Miyanishi, M. Yabashi, T. Togashi, K. Tono, O. Sakata, Y. Tange, K. Arakawa, Y. Ito, T. Okuchi, T. Sato, T. Sekine, T. Mashimo, N. Nakanii, Y. Seto, M. Shigeta, T. Shobu, Y. Sano, T. Hosokai, T. Matsuoka, T. Yabuuchi, K. A. Tanaka, N. Ozaki, and R. Kodama, *Sci. Rep.* **13**, 13796 (2023).
- ¹⁸J. C. Crowhurst, M. R. Armstrong, K. B. Knight, J. M. Zaugg, and E. M. Behymer, *Phys. Rev. Lett.* **107**, 144302 (2011).
- ¹⁹I. Nishibata, N. Nakanii, and T. Sano, *Opt. Cont.* **2**, 1735 (2023).
- ²⁰E. G. Gamaly, *Phys. Rep.* **508**, 91–243 (2011).
- ²¹V. H. Whitley, S. D. McGrane, D. E. Eakins, C. A. Bolme, D. S. Moore, and J. F. Bingert, *J. Appl. Phys.* **109**, 013505 (2011).
- ²²B. J. Demaske, V. V. Zhakhovskiy, N. A. Inogamov, and I. I. Oleynik, *Phys. Rev. B* **87**, 054109 (2013).
- ²³Y. B. Zeldovich and Y. P. Raizer, *Physics of Shock Waves and High Temperature Hydrodynamic Phenomena* (Academic Press, 1967).
- ²⁴M. Bhowmick, W. P. Basset, S. Matveev, L. Salvati, and D. D. Dlott, *AIP Adv.* **8**, 125123 (2018).
- ²⁵A. Benuzzi-Mounaix, M. Koenig, J. M. Boudenne, T. A. Hall, D. Batani, F. Scianitti, A. Masini, and D. Di Santo, *Phys. Rev. E* **60**, R2488–R2491 (1999).
- ²⁶A. C. Mitchell and W. J. Nellis, *J. Appl. Phys.* **52**, 3363–3374 (1981).
- ²⁷W. J. M. Rankine, *Phil. Trans. R. Soc. London* **160**, 277–288 (1870).
- ²⁸P. H. Hugoniot, *J. Ec. Polytech.* **57**, 3–97 (1887).
- ²⁹P. B. Corkum, F. Brunel, N. K. Sherman, and T. Srinivasan-Rao, *Phys. Rev. Lett.* **61**, 2886–2889 (1988).
- ³⁰A. Ng, A. Forsman, and P. Celliers, *Phys. Rev. E* **51**, R5208–R5211 (1995).
- ³¹V. V. Zhakhovskiy, M. M. Budzevich, N. A. Inogamov, I. I. Oleynik, and C. T. White, *Phys. Rev. Lett.* **107**, 135502 (2011).
- ³²V. V. Zhakhovskii and N. A. Inogamov, *JETP Lett.* **92**, 521–526 (2010).
- ³³N. Egashira, T. Matsuda, T. Okuchi, Y. Seto, Y. Ito, T. Shobu, N. Nakanii, Y. Inubushi, T. Togashi, K. Miyanishi, T. Mashimo, and T. Sano, *J. Appl. Phys.* **137**, 105903 (2025).
- ³⁴M. A. Meyers, *Scr. Metall.* **12**, 21–26 (1978).